frontiers in Physics

ORIGINAL RESEARCH
published: 03 March 2022
doi: 10.3389/fphy.2022.853179

Sm-Eu Co-Doped $BiFeO_3$ Nanoparticles With Superabsorption and Electrochemical Oxygen Evolution Reaction

Yanhong Gu[1], Niu Huang[2], Chaoyang Guo[1], Yuanxi Liang[1], Weiying Zhang[1], Jianguo Zhao[1], Xianghui Zhang[1], Hong Jia[1]* and Wanping Chen[3]*

[1]School of Physics and Electronic Information and Key Lab Electromagnet Transformation and Detect Henan, Luoyang Normal College, Luoyang, China, [2]Key Laboratory of Inorganic Nonmetallic Crystalline and Energy Conversion Materials, College of Materials and Chemical Engineering, China Three Gorges University, Yichang, China, [3]Key Laboratory of Artificial Micro- and Nano-Structures of Ministry of Education and School of Physics and Technology, Wuhan University, Wuhan, China

$Bi_{0.95}Sm_{0.05}Fe_{1-x}Eu_xO_3$ (x = 0, 0.05, 0.10, 0.15) nanoparticles were prepared via a two-solvent sol–gel method. The X-ray diffraction (XRD) and Raman results suggested that the main phase of the samples gradually evolved from perovskite phase *R3c* to orthorhombic phase *Pbnm* with increasing Eu content and that the optical band gap gradually narrowed from 2.09 to 1.70 eV. Along with the structural change, the ferromagnetic properties were transformed, and interesting double hysteresis loops were observed for the sample where $x = 0.1$. All the bismuth ferrite (BFO) samples demonstrated extremely strong adsorbability, with the adsorption rate of refractory methyl orange reaching 90% in 5 min. These samples also exhibited superior oxygen evolution reaction (OER) performance, with a desirable onset potential of approximately 1.50 V vs. RHE. For the sample where $x = 0.15$, to support a current density of 100 mA/cm^2, an overpotential of only 294 mV was required, which is much better than that of pure Ni foam (330 mV). More experiments are needed to verify and explore the source and mechanism of the OER performance.

Keywords: $BiFeO_3$, energy gap, ferromagnetism, super absorption, oxygen evolution reaction (OER)

OPEN ACCESS

Edited by:
Sugata Chowdhury, National Institute of Standards and Technology (NIST), United States

Reviewed by:
Rahul Kumar, Indian Institute of Technology Delhi, India
Khian-Hooi Chew, University of Malaya, Malaysia

****Correspondence:***
Niu Huang
huangliu.ysxf@163.com
Hong Jia
jiahong517@aliyun.com

Specialty section:
This article was submitted to Physical Chemistry and Chemical Physics, a section of the journal Frontiers in Physics

Received: *12 January 2022*
Accepted: *02 February 2022*
Published: *03 March 2022*

Citation:
Gu Y, Huang N, Guo C, Liang Y, Zhang W, Zhao J, Zhang X, Jia H and Chen W (2022) Sm-Eu Co-Doped $BiFeO_3$ Nanoparticles With Superabsorption and Electrochemical Oxygen Evolution Reaction. Front. Phys. 10:853179. doi: 10.3389/fphy.2022.853179

INTRODUCTION

In recent years, owing to the magnetoelectric coupling effect, multiferroic materials have been widely applied in the fields of information storage, electronic devices, and sensors, and thus they have attracted extensive attention from researchers worldwide. Bismuth ferrite ($BiFeO_3$, or BFO) stands out among multiferroic material because of its ferromagnetism and ferroelectricity at room temperature [1, 2]. BFO can also be used as a photocatalyst to degrade organic pollutants and decompose water because it is a semiconductor material with a narrow band gap (2.2 eV) and excellent chemical stability [3, 4].

At present, there are two popular ways to decompose water: photocatalytic decomposition and electrocatalytic decomposition. The electrocatalytic decomposition of water involves two reactions: the anodic oxygen evolution reaction (OER) and the cathodic hydrogen evolution reaction (HER), both of which are related to electrocatalysts. OER is the key reaction in energy storage processes, such as water cracking and metal–air batteries [5]. However, it is difficult to carry out because it involves four proton-coupled electron transfer processes, and so it requires a very high overpotential to

complete the process [6]. At present, IRO_x/RuO_x and Pt/C are the benchmark electrocatalysts for OER and HER, respectively. Although these electrocatalysts exhibit high electrocatalytic activity and kinetics, their high cost, scarcity, and unsatisfactory electrochemical stability prevent them from being widely used. In recent years, many efforts have been made to design low-cost, high-catalytic, stable, and environmentally friendly non-noble metal or carbon-based electrocatalysts. Perovskite oxides (ABO_3–δ) have been widely studied as electrocatalysts owing to their composition and structural flexibility [7–10]. Perovskite oxides (ABO_3) also have a variety of structures and physical and chemical properties, which have attracted considerable interest for use in OER. The perovskite oxide BFO is a multiferroic functional material, as well as a ferroelectric semiconductor that facilitates the separation of electrons and holes, and thus BFO is increasingly being investigated for applications in solar energy conversion and for designing desired electrocatalysts.

BFO has made many representative achievements in catalytic performance and energy storage of fuel cells [11–13]. The application and development of BFO as a supercapacitor has also achieved a lot of fruitful work [14–18]. $Bi_{0.15}Sr_{0.85}Co_{0.8}Fe_{0.2}O_{3-\delta}$ presents a low OER overpotential (354 mV at 10 mA cm^{-2}) and good reaction kinetics for both OER and ORR (94.21 mV dec^{-1} and 72.5 mV dec^{-1}, respectively) [19]. The current density for the OER of $Bi_{0.6}Ca_{0.4}FeO_3$ showed a significantly high value of 6.93 mA/cm^2 at a fixed overpotential of 0.42 V (1.65 V vs. RHE) [20]. A 15% Ca-doped $Bi_{0.85}Ca_{0.15}FeO_3$ catalyst showed an increased kinetic current density of 54.562 mA/cm^2 at an onset potential of 2.122 (V vs. RHE) with an overpotential of 0.892 V in an alkaline electrolyte [21]. All of these tests are performed on glassy carbon, but surface chemistry is an important prerequisite for advanced water electrolysis. The excellent specific surface area of nickel foam has not been fully utilized to demonstrate the OER performance of BFO. The porous structure of the Ni foam can expose more active sites of the material.

In this work, Sm and Eu are chosen for co-doping into the BFO host materials. Because Sm doped $BiFeO_3$ can improve magnetic and electric properties [12]. Eu substitution for the Fe-site is expected to modulate structure and band gap width to a greater extent resulting in a good water decomposition and electrocatalytic performance [22, 23]. Herein, we report a simple and feasible method for the fabrication of perovskite $BiFeO_3$ photoanodes. Sm and Eu co-doped $BiFeO_3$ nanoparticles were fabricated by a double sol–gel method. With increasing Eu content, the BFO structure changed from perovskite to orthorhombic, as demonstrated by both X-ray diffraction (XRD) and Raman patterns. Interestingly, the Sm and 15% Eu co-doped $BiFeO_3$ had a strong adsorption performance, and the adsorption rate of methyl orange reached 95% in 5 min. The electrocatalytic performance was also superior, such that at an onset potential of 1.48 V vs. RHE, the overpotential was merely 294 and 310 mV to support current densities of 100 mA/cm^2 and 400 mA/cm^2, respectively. BFO is a multifunctional composite material. It is therefore hoped that the electrochemical properties of BFO can be further studied using its ferroelectric and ferromagnetic properties.

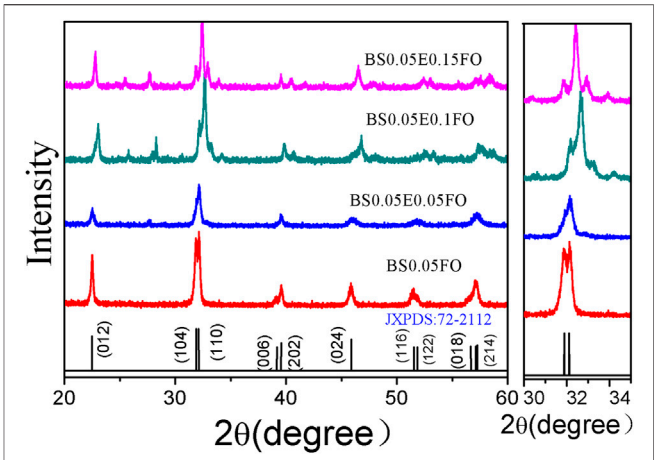

FIGURE 1 | XRD patterns of the $Bi_{0.95}Sm_{0.05}Fe_{1-x}Eu_xO_3$ (x = 0.0, 0.05, 0.10, 0.15) ceramic samples, with enlarged views of the (104) and (110) diffraction peaks near the diffraction angle 2θ = 32°.

EXPERIMENTAL

Synthesis of Sm and Eu Co-Doped $BiFeO_3$

$BiFeO_3$ and $Bi0_{.95}Sm_{0.05}Fe_{1-x}Eu_xO_3$ (BSFEO) (x = 0.0, 0.05, 0.10, 0.15) nanoparticles, denoted as BFO, BSFO, BSFO–5Eu, BSFO–10Eu, and BSFO–15Eu, respectively, were synthesized by the double-solvent sol–gel method. $Bi(NO_3)_3{\cdot}5H_2O$ (99% pure) and $Sm(NO_3)_3{\cdot}6H_2O$ (99.9% pure) were mixed stoichiometrically, dissolved in ethylene glycol ($C_2H_6O_2$), and stirred for 90 min at room temperature (RT). $Fe(NO_3)_3{\cdot}9H_2O$ (98.5% pure) and $Eu(NO_3)_3{\cdot}6H_2O$ (98.5% pure) powders were dissolved in acetic acid and magnetically stirred for 1.5 h. Subsequently, the two solutions were mixed and stirred continuously for 3 h, resulting in a homogeneous, reddish-brown, and fine precursor solution (0.4 M). Because of the bismuth loss during heating, an excess of 3% bismuth was added to the solution to compensate. To maintain the electronegativity of the iron and bismuth during the chemical reactions, ethylene glycol was added as a solvent. In the synthesis process, acetic acid was used as a catalyst to control the chemical reaction and maintain the concentration of the solution. The prepared solution was dried in an oven at 80°C for a few days to obtain a gel, which was then ground into a fine powder and calcined in an oven at 600°C for 3 h to remove the organic matter. Subsequently, it was ground again and cleaned with dilute nitric acid. The BSFEO samples were prepared after a few hours of drying.

Materials Characterization

XRD and Raman scattering spectroscopy were used to characterize the structures of the samples. Scanning electron microscopy (SEM) was used to determine the morphology and

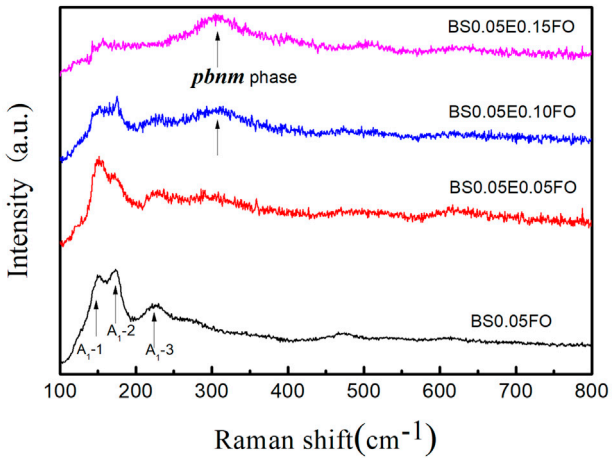

FIGURE 2 | Raman spectra as a function of Eu composition.

granularity of the prepared samples. The ultraviolet-visible (UV-vis) diffuse reflectance spectra of the prepared samples were studied using a UV-vis spectrophotometer, and the band gap width was studied. The ferromagnetic properties of the samples in the magnetic field range of −20 to 20,000 KOe were investigated using a vibrating sample magnetometer (VSM) at RT. The N_2 adsorption–desorption isotherms were measured using an ASAP 2020 Plus HD88 gas adsorption and porosity meter at a liquid nitrogen temperature of −196°C. Before the experiment, the sample was degassed at 140°C for 3 h. The Barrett–Joyner–Halenda (BJH) method was used to obtain the distribution curve of the pore size. All electrochemical measurements were conducted using an electrochemical workstation (CHI760E, Chenhua).

OER Characterization

The catalyst ink was prepared by dissolving 5 mg of catalyst in 1.96 ml of deionized water and ethyl alcohol in a volume ratio of 1:1, after which 40 μl of Nafion® was added. The mixture was sonicated for 30 min to form a homogenous ink. Next, 0.4 ml of ink was dropped onto the surface of Ni foam (NF, with surface area of 1 cm^2). After drying naturally at RT, the BSFEO/NF series were prepared. The electrochemical OER was carried out using a three-electrode system on an electrochemical workstation (CHI760E) with a catalyst coated on glassy carbon (GC) or NF as the working electrode, carbon rods, and saturated Hg/HGO electrodes as the counter and reference electrodes, respectively. OER tests were performed in an O_2-saturated 1 M KOH electrolyte at RT at a scanning rate of 5 mV/s. Infrared compensation was applied for calibration in the linear sweep voltammetry (LSV) tests, and a reversible hydrogen electrode (RHE) was used to adjust the working potential.

RESULTS AND DISCUSSION

Figure 1 shows the XRD patterns of the $Bi_{0.95}Sm_{0.05}Fe_{1-x}Eu_xO_3$ (x = 0.0, 0.05, 0.10, 0.15) nanoparticles and the distorted rhombohedral structures with an *R3c* space group. The doubly split peaks of BFO in the 2θ range of 31–33° merge to a single peak upon doping with Eu, and two smaller peaks formed on each side, which became higher as the doping proportion increased. These analyses indicate that the crystallinity of the BFO powder was considerably affected by doping with Eu. In addition, at x = 0.15 and 0.2, the diffraction peaks in the 2θ range of 38–40° split, and there were some changes in other peaks. Previous research has shown that an orthorhombic structure can be transformed during element substitution [24, 25], thus the unit-cell symmetry of BSFEO shifted from *R3c* to *Pbnm* with increasing Eu content.

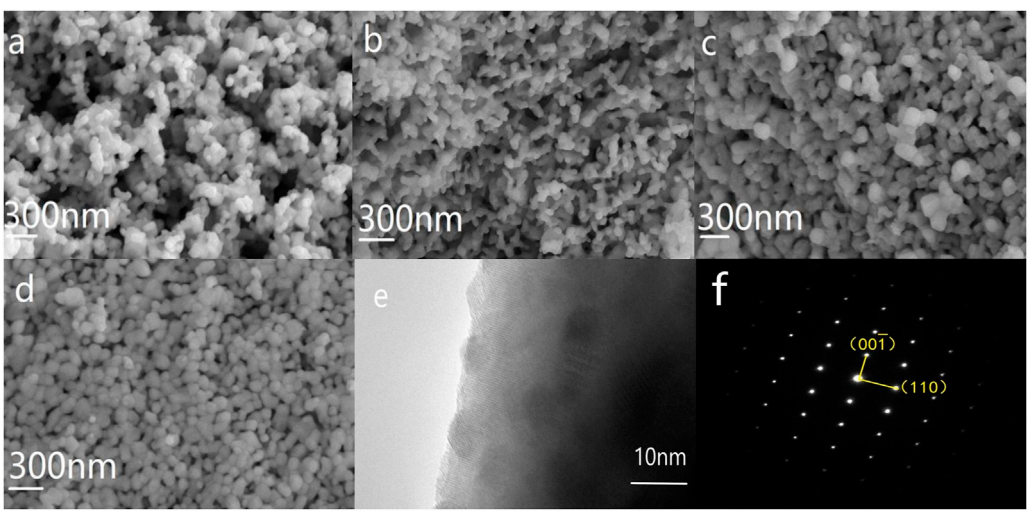

FIGURE 3 | SEM images of BSFO powders doped with Eu at ratios of **(A)** 0.0, **(B)** 0.05, **(C)** 0.10, and **(D)** 0.15. TEM images of BSFO–15Eu nanoparticles **(E)**, and **(F)** shows the SAED of BSFO–15Eu nanoparticles and the belt axis is [1¯00].

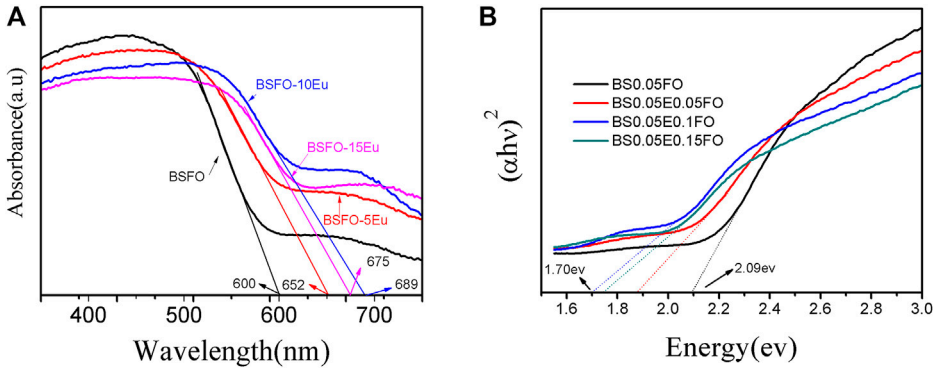

FIGURE 4 | (A) UV-vis diffuse reflectance spectrum of the BSFO, BSFO–5Eu, BSFO–10Eu, and BSFO–15Eu nanoparticles, **(B)** the calculation of band gap.

TABLE 1 | The band gap width of BSFEO.

Doping content	λ/nm	E_g/eV
0	600	2.07
BSFO-5Eu	652	1.90
BSFO-10Eu	689	1.80
BSFO-15Eu	675	1.84

For a more detailed view of the structural changes, the Raman spectra, which confirm the XRD results, are shown in **Figure 2**. It is well known that perovskite BFO has nine vibration modes, namely, four strong peaks (A_1-1, A_1-2, A_1-3, and A_1-4 modes) and six weak peaks (E-2, E-3, E-4, E-5, E-6, and E-7 modes) [26]. It is obvious from the Raman results that with the addition of Eu, the peak of the main vibration mode of the perovskite structure gradually weakened. In contrast, a new mode at 310 cm^{-1} became gradually more pronounced, which was caused by the A-site vibration and the oxygen sloping of the *Pbnm* orthorhombic structure [26, 27]. The Raman results again proved that the Sm and Eu co-doped BFO system evolved from an *R3c* to a *Pbnm* structure. It is noted that for BSFEO nanoparticles with doping contents of 0.10 and 0.15, the peak at 310 cm^{-1} was very pronounced.

To fully understand the properties and morphological characteristics of the Eu and Sm co-doped BFO nanoparticles, SEM images of BSFEO powders with various doping contents are shown in **Figure 3**. It can be seen that the characteristics of agglomeration and surface structure are becoming more conspicuous and homogeneous with increasing Eu substitution concentration. Upon further increasing the Eu content, the grain size of the samples continued to increase. The average grain size increased from 30 to 50 μm at $x = 0$ to 50–70 μm at $x = 0.15$. More importantly, the distance between the particles decreased with increasing doping content. The excellent magnetic properties of BFO are related to its surface structure. The tighter the BFO lattice system, the more difficult it is for the O and Bi elements to escape. The elevation in the potential magnetic properties of BFO can be explained by the reduction in the number of oxygen vacancies and the helical structure owing to the dense surface structure. TEM image of BSFO–15Eu nanoparticles are shown in **Figures 3E,F**. It is evident from TEM images that the crystallinity of the sample was very good and clear diffraction spots can be seen, and the diffraction patterns of these spots agree well with the orthorhombic phase Pbnm of BFO, which is also consistent with the XRD results. The axial direction of the diffraction spot is [$\bar{1}$ 00].

Figure 4 shows the UV-vis peaks of BSFEO nanoparticles with various doping contents. It is clear that a spectrum shift occurred when BSFO was doped with Eu, which increased the band gap. According to the data in **Table 1**, the cut-off absorption wavelength of BSFEO nanoparticles in this experiment was approximately 1.90 nm and the minimum was 1.80 eV. By comparing the data, it was found that as the doping ratio increased, the band gap width decreased. This increase in band gap may result in improved magnetic and electrocatalytic

TABLE 2 | OER performances of NF and BSFEO coated on NFs.

Sample	Onset potential (V vs. RHE)	η_j = 10 mA cm^{-2} (mV)	η_j = 100 mA cm^{-2} (mV)	η_j = 400 mA cm^{-2} (mV)	Tafel slope (mV dec^{-1})
NF	1.48	282	332	366	52
BSFO-5Eu	1.47	276	322	352	43.4
BSFO-10Eu	1.47	262	306	328	42
BSFO-15Eu	1.46	254	295	316	38

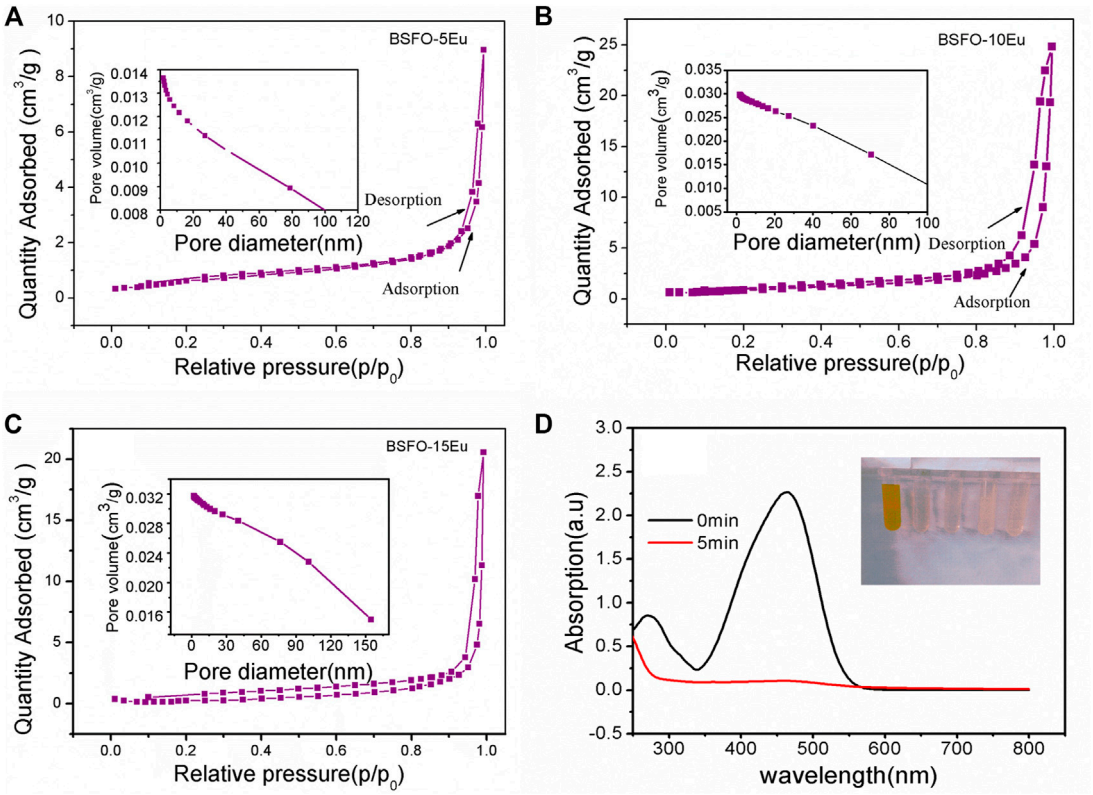

FIGURE 5 | N_2 adsorption–desorption isotherms and the corresponding pore-size distribution curves (inset) of the as-prepared samples: **(A)** BSFO-5Eu, **(B)** BSFO-10Eu, and **(C)** BSFO-15Eu. **(D)** Adsorption effect of methyl orange of BSFO-5Eu.

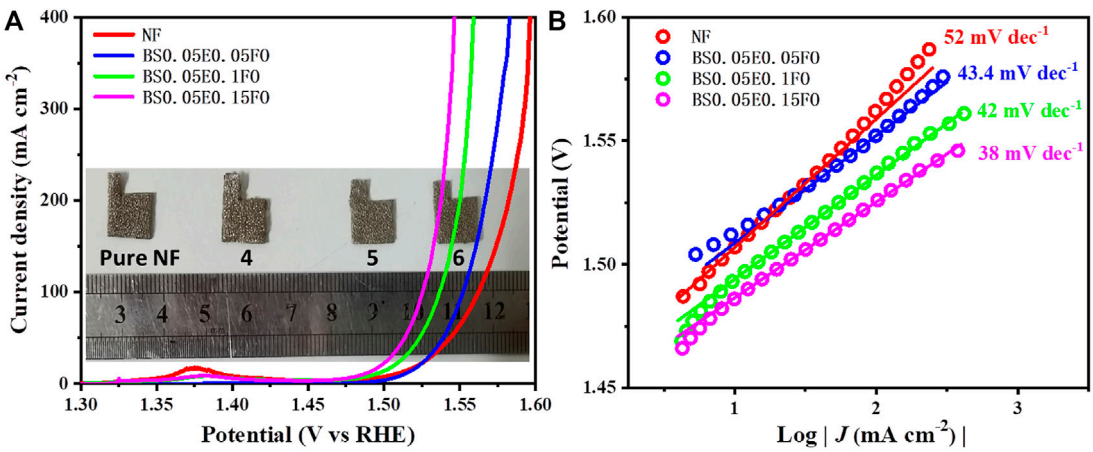

FIGURE 6 | (A) Polarization curves and **(B)** corresponding Tafel plots of NF and $Bi_{0.95}Sm_{0.05}Fe_{1-x}Eu_xO_3$ ($x = 0.05, 0.10, 0.15$) samples deposited on NFs, with their digital photos inserted in **(A)**.

performance of the BSFEO nanoparticles. Our results indicate that the BSFEO band gap can be tuned by increasing the doping ratio to increase the range of electrocatalytic and magnetic properties.

As an important structural parameter, the surface area may affect the OER. The specific surface areas of the prepared samples were determined by N_2 adsorption–desorption isotherms. The isotherms and pore-size distribution curves of the BSFO-5Eu,

TABLE 3 | Comparison of OER activity for different.

Catalyst	Electrolytes	η_j = 10 mA cm^{-2} (mV)	Tafel slope (mV dec^{-1})	Substrate	Reference
$BiSm_{0.05}Eu_{0.15}FeO_3$	1.0 m KOH	254	38	Ni foam	This work
$LaCoO_3$-80 nm	1.0 m KOH	490	69	GCE	[8]
$Ba_{0.5}Sr_{0.5}Co_{0.8}Fe_{0.2}O_3$	1.0 m KOH	500	94	GCE	[17]
$SrNb_{0.1}Co_{0.7}Fe_{0.2}O_3$	1.0 m KOH	500	76	GCE	[17]
NiFe LDH@NiCoP	1.0 m KOH	220	48.6	Ni foam	[18]
$NiCo_2O_4$ NPs	1.0 m KOH	240	50	Ni foam	[19]
Mn_3N_2	1.0 m KOH	270	101	Ni foam	[20]
$CoFe_2O_4$ nanorod array	1.0 m KOH	240	45	Ni foam	[21]
CoFe LDHs nanosheets	1.0 m KOH	232	36	Ni foam	[22]

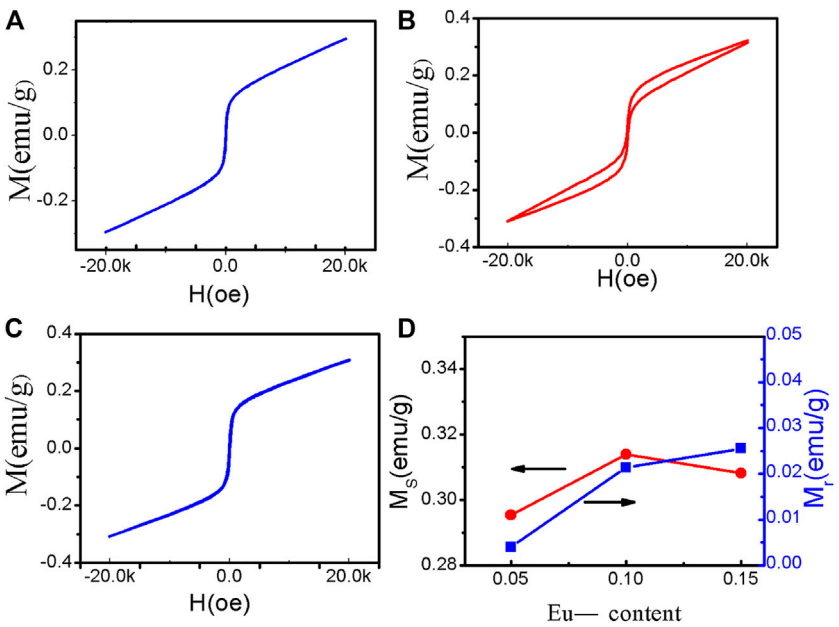

FIGURE 7 | Magnetic hysteresis loops of the nanoparticles at RT: **(A)** BSFO–5Eu, **(B)** BSFO–10Eu, and **(C)** BSFO–15Eu. **(D)** Eu-substituted concentration dependencies of M_r and M_s.

BSFO-10Eu, and BSFO-15Eu samples are shown in **Figure 5**. The Brunauer–Emmett–Teller (BET) results demonstrated that the specific surface areas for the powder samples were 2.47, 3.26, and 0.90 m^2/g for the BSFO–5Eu, BSFO–10Eu, and BSFO–15Eu samples, respectively, indicating that the surface area did not directly affect the OER performance. It therefore seems that the specific surface area did not play a decisive role in OER. However, the average pore size of the three samples were 6.8, 24, and 31 nm for the BSFO–5Eu, BSFO–10Eu, and BSFO–15Eu samples. Generally speaking, large pores are conducive to the transmission of media in the absence of stirring. The larger the pore, the more conducive to mass transfer results in the improvement of OER performance in electrocatalysis.

The OER performance of the Sm and Eu co-doped BFO series was measured via LSV. As shown in **Figure 6A**, the BSFEO samples all exhibited favorable electrocatalytic activity toward OER superior to that of NF. It is worth noting that the onset potential was small at 1.46 V vs. RHE (**Figure 6A**). To achieve a current density of 100 mA cm^2, the corresponding overpotentials were 295, 306, 322, and 332 mV for BSFO–15Eu, BSFO–10Eu, BSFO–5Eu and NF, respectively. To achieve a current density of 400 mA cm^2, the corresponding required overpotentials were 316, 328, 352, and 366 mV for BSFO–15Eu, BSFO–10Eu, BSFO–5Eu, and NF, respectively. **Figure 6B** shows the corresponding Tafel plots, wherein all BSFEO samples exhibit fast OER kinetics with extremely small Tafel slopes. In particular, the slope of BSFO–15Eu is 38 mV dec^{-1} and relatively small, indicating that its OER dynamic process was the fastest and most powerful. Detailed data on OER are shown in **Table 2**. These results suggest that BSFEO possesses excellent OER performance, comparable to those of $LaCoO_3$ series [8, 10], $Ba_{0.5}Sr_{0.5}Co_{0.8}Fe_{0.2}O_{3-\delta}$ [28], NiFe-LDH [29], $NiCo_2O_4$ [30],

Mn_3N_2 [31], $CoFe_2O_4$ [32] and CoFe-LDH [33] nanosheets, as shown in **Table 3**.

There are two theories about the OER origin of perovskite ABO3. One is that an oxygen vacancy is the active site, and the other is B-site transition metal ions. In our system, because both Sm and Eu elements are trivalent, there is no tendency to introduce oxygen vacancies according to the principle of defect chemical equilibrium. In other words, all samples contain the same amount of oxygen vacancies. Therefore, the transition metal at the B site serves as the active site in our system, and it can be seen from the above experimental results that Eu or Fe is the active site. The specific OER reaction process is as follows:

$$OH^- + M \rightleftarrows MOH + e^-$$
$$MOH + OH^- \rightleftarrows MO + H_2O + e^-$$
$$MO + OH^- \rightleftarrows MOOH + e^-$$
$$MOOH + OH^- \rightleftarrows O_2 + H_2O + e^- + M$$

The magnetic hysteresis (M-H) loops of the samples are shown in **Figure 7**, where both the remanent magnetization (M_r) and saturation magnetization (M_s) increased significantly with increasing Eu substitution content. The values of M_s for BSFO–5Eu, BSFO–10Eu, and BSFO–15Eu were 0.29, 0.31, and 0.308 emu/g, respectively. The values of M_r for BSFO, BSFO–5Eu, BSFO–10Eu, and BSFO–15Eu were 0.004, 0.021, and 0.0256 emu/g, respectively. This comes from the substitution-driven modification of the spiral G-type antiferromagnetic ordering, which is characteristic of BFO, to the collinear G-type antiferromagnetic structure, in which the canted component of the antiferromagnetically ordered spins becomes measurable. That is to say, this enhancement of the ferromagnetism was attributed to the structural distortion, which modulates the canted spin structure and change the Fe–O–Fe angle. It was expected that this structural distortion could lead to suppression of the spin spiral and hence enhanced the magnetization [12].

Interestingly, double ferromagnetic hysteresis loops were observed in the Sm and Eu co-doped samples. In particular, the BSFO–10Eu sample had the most obvious double ferromagnetic hysteresis loop, which is located at the coexistence phase of the *R*3*C* and *Pnma* phases. The double ferromagnetic hysteresis loop of BFO systems has rarely been reported or observed. In general, double hysteresis loops are caused by the coexistence of hard/permanent magnets and soft magnets or antiferromagnetic and ferromagnetic phases [34–36]. In the Eu and Sm co-doped BFO system, the two different magnetic phases may be associated with the ferromagnetic *Pnma* phase and antiferromagnetic *R*3*C* phase. Increasing the response efficiency of OER using a magnetic field as a new regulatory approach has recently attracted widespread attention. Ren et al. showed the spin-polarized kinetics of the OER [37, 38].

CONCLUSION

In summary, BSFEO powders with various doping contents were synthesized using sol–gel technology. With increasing Eu content, the XRD spectra showed that the structure transitioned from the *R*3*C* phase to the *Pnma* phase. The diameters of the Eu-doped particles increased and the distances between them significantly decreased. The peak of the Raman spectra at 136 cm^{-1} clearly decreased, and the peak at 310 cm^{-1} significantly increased. The band gap width was in the range of 1.80–2.07 eV. A comparison of the data showed that the M_s and M_r values for the Eu-doped samples improved. Simultaneously, all the samples exhibited superior OER performance, with a desirable onset potential of approximately 1.50 V vs. RHE. For the sample in which x = 0.15, to support a current density of 100 mA/cm^2, an overpotential of only 294 mV was required, which is much better than that of pure NF (330 mV). The reason and mechanism of OER performance are being systematically studied.

DATA AVAILABILITY STATEMENT

The original contributions presented in the study are included in the article/Supplementary Material, further inquiries can be directed to the corresponding authors.

AUTHOR CONTRIBUTIONS

CG and YL implementation of samples preparation; JZ and WZ implementation of resource and suggestion; WC implementation of modifying and editing.

FUNDING

This work was supported by the Program for Young Teachers of Higher School in Henan Province (2019GGJS197).

REFERENCES

1. Catalan G, Scott JF. Physics and Applications of Bismuth Ferrite. *Adv Mater* (2009) 21(24):2463–85. doi:10.1002/adma.200802849
2. Eerenstein W, Mathur ND, Scott JF. Multiferroic and Magnetoelectric Materials. *Nature* (2006) 442(7104):759–65. doi:10.1038/nature05023
3. Yang Y, Kang L, Li H. Enhancement of Photocatalytic Hydrogen Production of $BiFeO_3$ by Gd^{3+} Doping. *Ceram Int* (2018) 45(6):8017–22. doi:10.1016/j.ceramint.2018.12.150
4. Vishwakarma AK, Tripathi P, Srivastava A, Sinha ASK, Srivastava ON. Band gap Engineering of Gd and Co Doped BiFeO3 and Their Application in Hydrogen Production through Photoelectrochemical Route. *Int J Hydrogen Energ* (2017) 42(36):22677–86. doi:10.1016/j.ijhydene.2017.07.153
5. Liu YA, Niu HA, Chan LA, Hy B, Ps A, Xl A, et al. Atomically Dispersed and Nanoscaled Co Species Embedded in Micro-/mesoporous Carbon Nanosheet/nanotube Architecture with Enhanced Oxygen Reduction and Evolution Bifunction for Zn-Air Batteries - ScienceDirect. *Chem Eng J* (2020) 404:127112. doi:10.1016/j.cej.2020.127112

6. Wu Z, Lu XF, Zang S, Lou X. Non-Noble-Metal-Based Electrocatalysts toward the Oxygen Evolution Reaction. *Adv.Funct.Mater* (2020) 30(15):1910274. doi:10.1002/adfm.201910274
7. Sun H, Dai J, Zhou W, Shao Z. Emerging Strategies for Developing High-Performance Perovskite-Based Materials for Electrochemical Water Splitting. *Energy Fuels* (2020) 34:10547–67. doi:10.1021/acs.energyfuels.0c02313
8. Zhou S, Miao X, Xu Z, Chao M, Qiu Y, Hu Z, et al. Engineering Electrocatalytic Activity in Nanosized Perovskite Cobaltite through Surface Spin-State Transition. *Nat Commun* (2016) 7(1):11510. doi:10.1038/ncomms11510
9. Badreldin A, Abusrafa AE, Abdel-Wahab A. Oxygen-deficient Perovskites for Oxygen Evolution Reaction in Alkaline media: a Review. *Emergent Mater* (2020) 3(5): 567–590. doi:10.1007/s42247-020-00123-z
10. Suntivich J, May KJ, Gasteiger HA, Goodenough JB, Shao-Horn Y. A Perovskite Oxide Optimized for Oxygen Evolution Catalysis from Molecular Orbital Principles. *Science* (2011) 334:1383–5. doi:10.1126/science.1212858
11. Anand P, Jaihindh DP, Chang W-K, Fu Y-P. Tailoring the Ca-Doped Bismuth Ferrite for Electrochemical Oxygen Evolution Reaction and Photocatalytic Activity. *Appl Surf Sci* (2021) 540:148387. doi:10.1016/j.apsusc.2020.148387
12. Thang DV, Hung NM, Hung NM, Khang NC, Oanh LTM. Structural and Multiferroic Properties of (Sm, Mn) Co-doped BiFeO3 Materials. *AIMS Mater Sci* (2020) 7(2):160–9. doi:10.3934/matersci.2020.2.160
13. Ma C-J, Li N, Song W-L. Tailoring the Electrochemical Behaviors of Bismuth Ferrite Using Ca Ion Doping. *Front Mater* (2020) 7:151–157. doi:10.3389/fmats.2020.00015
14. Soam A, Kumar R, C M, Singh M, Thatoi D, Dusane RO. Development of Paper-Based Flexible Supercapacitor: Bismuth Ferrite/graphene Nanocomposite as an Active Electrode Material. *J Alloys Compd* (2020) 813:152145. doi:10.1016/j.jallcom.2019.152145
15. Nayak S, Soam A, Nanda J, Mahender C, Singh M, Mohapatra D, et al. Sol-gel Synthesized BiFeO3-Graphene Nanocomposite as Efficient Electrode for Supercapacitor Application. *J Mater Sci Mater Electron* (2018) 29(11): 9361–8. doi:10.1007/s10854-018-8967-6
16. Ankur Soam A, Kumar R, Singh M. Electrophoretically Deposited Bismuth Iron Oxide Nanoparticles Film for Supercapacitor Application. *Russ J Electrochem* (2020) 56(12):1037–42. doi:10.1134/s1023193520120241
17. Soam A, Kumar R, Thatoi D, Singh M. Electrochemical Performance and Working Voltage Optimization of Nickel Ferrite/graphene Composite Based Supercapacitor. *J Inorg Organomet Polym* (2020) 30(9):3325–31. doi:10.1007/s10904-020-01540-7
18. Soam A, Mahender C, Kumar R, Singh M. Power Performance of BFO-Graphene Composite Electrodes Based Supercapacitor. *Mater Res Express* (2018) 6(2):025054. doi:10.1088/2053-1591/aaf125
19. Jing LA, Fan YA, Yd A, Xc A, Qh B, Jz A, Bi0.15Sr0.85Co0.8Fe0.2O3- perovskite: A novel bifunctional oxygen electrocatalyst with superior durability in alkaline media, 108 (2021) 158–63. doi:10.1016/j.jmst.2021.09.027
20. Afzal RA, Park K-Y, Cho S-H, Kim N-I, Choi SR, Kim JH, et al. Oxygen Electrode Reactions of Doped BiFeO3 Materials for Low and Elevated Temperature Fuel Cell Applications. *RSC Adv* (2017) 7(75):47643–53. doi:10.1039/c7ra08671g
21. Jaihindh DP, Fu YP, Pandiyarajan A. Tailoring the Ca-Doped Bismuth Ferrite for Electrochemical Oxygen Evolution Reaction and Photocatalytic Activity. *Appl Surf Sci* (2020) 540:148387. doi:10.1016/j.apsusc.2020.148387
22. Hu Z, Li M, Liu J, Pei L, Wang J, Yu B, et al. Structural Transition and Multiferroic Properties of Eu-Doped BiFeO3 Thin Films. *J Am Ceram Soc* (2010) 93(9):2743–7. doi:10.1111/j.1551-2916.2010.03766.x
23. Zhu Y, Quan C, Ma Y, Wang Q, Mao W, Wang X, et al. Effect of Eu, Mn Co-doping on Structural, Optical and Magnetic Properties of BiFeO 3 Nanoparticles. *Mater Sci Semiconductor Process* (2017) 57:178–84. doi:10.1016/j.mssp.2016.10.023
24. Yuan GL, Or SW, Liu JM, Liu ZG. Structural Transformation and Ferroelectromagnetic Behavior in Single-phase Bi1−xNdxFeO3 Multiferroic Ceramics. *Appl Phys Lett* (2006) 89(5):052905. doi:10.1063/1.2266992
25. Zhang S, Luo W, Wang D, Ma Y. Phase Evolution and Magnetic Property of Bi1−xDyxFeO3 Ceramics. *Mater Lett* (2009) 63(21):1820–2. doi:10.1016/j.matlet.2009.05.056
26. Fukumura H, Harima H, Kisoda K, Tamada M, Noguchi Y, Miyayama M. Raman Scattering Study of Multiferroic BiFeO3 Single crystal. *J Magnetism Magn Mater* (2007) 310(2):e367–e369. doi:10.1016/j.jmmm.2006.10.282
27. Ke H, Zhang L, Zhang H, Li F, Luo H, Cao L, et al. Electric/magnetic Behaviors of Nd/Ti Co-doped BiFeO3 Ceramics with Morphotropic Phase Boundary. *Scripta Materialia* (2019) 164:6–11. doi:10.1016/j.scriptamat.2019.01.025
28. Zhu Y, Zhou W, Chen Z-G, Chen Y, Su C, Tadé MO, et al. SrNb0.1Co0.7Fe0.2O3−δPerovskite as a Next-Generation Electrocatalyst for Oxygen Evolution in Alkaline Solution. *Angew Chem* (2015) 127:3969–73. doi:10.1002/ange.201408998
29. Zhang H, Li X, Hähnel A, Naumann V, Lin C, Azimi S, et al. Bifunctional Heterostructure Assembly of NiFe LDH Nanosheets on NiCoP Nanowires for Highly Efficient and Stable Overall Water Splitting. *Adv Funct Mater* (2018) 28(14):1706847. doi:10.1002/adfm.201706847
30. Shengjie P, Feng G, Linlin L, Deshuang Y, Dongxiao J, Zhang T, et al. Necklace-like Multishelled Hollow Spinel Oxides with Oxygen Vacancies for Efficient Water Electrolysis. *J Am Chem Soc* (2018) 140(42): 13644–13653. doi:10.1021/jacs.8b05134
31. Driess M, Walter C, Menezes PW, Lerch M, Orthmann S, Kaiser B, et al. A Molecular Approach to Manganese Nitride Acting as a High Performance Electrocatalyst in the Oxygen Evolution Reaction. *Angew Chem* (2018) 130(3): 706–710. doi:10.1002/ange.201710460
32. Lu XF, Gu LF, Wang JW, Wu JX, Liao PQ, Li GR. Bimetal-Organic Framework Derived CoFe2 O4/C Porous Hybrid Nanorod Arrays as High-Performance Electrocatalysts for Oxygen Evolution Reaction. *Adv Mater* (2017) 29(3): 1604437. doi:10.1002/adma.201604437
33. Liu R, Wang Y, Liu D, Zou Y, Wang S. Water-Plasma-Enabled Exfoliation of Ultrathin Layered Double Hydroxide Nanosheets with Multivacancies for Water Oxidation. *Adv Mater* (2017) 29(30):1701546. doi:10.1002/adma.201701546
34. Gu Y, Zhou Y, Zhang W, Guo C, Zhang X, Zhao J, et al. Optical and Magnetic Properties of Sm-Doped BiFeO3 Nanoparticles Around the Morphotropic Phase Boundary Region. *AIP Adv* (2021) 11(4):045223. doi:10.1063/5.0042485
35. Shen L, Luo M, Liu Y, Liang R, Jing F, Wu L. Noble-metal-free MoS2 Co-catalyst Decorated UiO-66/CdS Hybrids for Efficient Photocatalytic H2 Production. *Appl Catal B: Environ* (2015) 166-167:445–53. doi:10.1016/j.apcatb.2014.11.056
36. Walker J, Simons H, Alikin DO, Turygin AP, Shur VY, Kholkin AL, et al. Dual Strain Mechanisms in a lead-free Morphotropic Phase Boundary Ferroelectric. *Sci Rep* (2016) 6:19630. doi:10.1038/srep19630
37. Ren X, Wu T, Sun Y, Li Y, Xu ZJ. Spin-polarized Oxygen Evolution Reaction under Magnetic Field. *Nat Commun* (2021) 12(1):1–12. doi:10.1038/s41467-021-22865-y
38. Sun Y, Sun S, Yang H, Xi S, Gracia J, Xu ZJ. Spin-Related Electron Transfer and Orbital Interactions in Oxygen Electrocatalysis. *Adv Mater* (2020) 32(39): 2003297. doi:10.1002/adma.202003297

Conflict of Interest: The authors declare that the research was conducted in the absence of any commercial or financial relationships that could be construed as a potential conflict of interest.

Publisher's Note: All claims expressed in this article are solely those of the authors and do not necessarily represent those of their affiliated organizations, or those of the publisher, the editors and the reviewers. Any product that may be evaluated in this article, or claim that may be made by its manufacturer, is not guaranteed or endorsed by the publisher.